



# The in situ grown of activated Fe-N-C nanofibers derived from polypyrrole on carbon paper and its electro-catalytic activity for oxygen reduction reaction

Min Sun<sup>1</sup> · Xiaobo Wu<sup>1,2</sup> · Chunbo Liu<sup>1</sup> · Zhiyong Xie<sup>1</sup> · Xiaoting Deng<sup>1</sup> · Wei Zhang<sup>1</sup> · Qizhong Huang<sup>1</sup> · Boyun Huang<sup>1</sup>

Received: 12 October 2017 / Revised: 4 December 2017 / Accepted: 8 December 2017 / Published online: 22 December 2017  
© Springer-Verlag GmbH Germany, part of Springer Nature 2017

## Abstract

The Fe-N-C nanofibers (NFs) exhibit excellent electro-catalytic activity for oxygen reduction reaction (ORR), which is essential for energy conversion system. Compared with the traditional ink-based electrode, we synthesized the structured Fe-N-C ANFs/CP (activated NFs derived from polypyrrole(PPy) doped with iron atoms in situ grown on carbon paper) by electrochemical polymerization. Herein, we investigate the effect of the iron concentration on the electro-catalytic activity for ORR, revealing that the as-prepared 0.05-Fe-N-C ANFs exhibit superior electro-catalytic activity than 0.01-Fe-N-C ANFs, 0.03-Fe-N-C ANFs as well as 0.10-Fe-N-C ANFs and excellent durability in alkaline solution. It is shown that the better electro-catalytic activity of 0.05-Fe-N-C ANFs for ORR could be ascribing to the fluffy fibrous structure, higher Fe-N<sub>x</sub> concentration, and well-dispersed catalytic active sites.

**Keywords** Polypyrrole · Activated nanofibers · Catalyst · Doping · Oxygen reduction reaction

## Introduction

Fuel cells have attracted tremendous attentions as an ideal and clean energy-converting devices with their excellent performances, such as high power density, high-efficiency, environmental friendliness and low emission [1–3]. However, the widely commercialized applications of the fuel cells have always been hindered due to their prohibitive-cost Pt-based catalysts and poor durability [4–7]. Thus, researchers have devoted themselves to exploit novel catalysts, namely noble-metal catalysts, and non-noble metal catalysts. For noble catalysts, alloy catalysts [5, 8],

catalyst structure and catalyst support innovation [5, 7, 9] are important aspects to use less (or no) precious metal Pt and increase Pt utilization, resulting in lowering the cost of fuel cells. As for non-noble metal catalysts, metal-N-C [6, 10–12] have drawn tremendous attentions from many researchers, holding great promise to substitute precious Pt-based catalysts used in fuel cells.

In fact, incorporating heteroatoms, such as nitrogen, boron, sulfur into carbon lattice seems to be an effective approach to improve the physical and chemical properties of carbon materials [13–17]. Reports show that the doped nitrogen atoms can significantly change the electronic structure of the carbon-nitrogen materials due to the electronegativity difference, resulting into the charge transfer, oxygen molecule adsorption mode transforming and the electro-catalytic activity enhancing, compared to intrinsic carbon materials [18, 19]. Among various kinds of carbon nanomaterials, one-dimensional nanofibers (NFs) hold great promise to serve as catalyst support as well as catalysts in fuel cells, and electrode materials in supercapacitor due to their large specific area, high electro-catalytic activity and relatively feasible preparation process [20, 21]. Traditionally, one-dimensional nanofibers can be synthesized by chemical vapour deposition (CVD),

✉ Zhiyong Xie  
xzy507@csu.edu.cn

<sup>1</sup> State Key Laboratory of Powder Metallurgy, Central South University, 932 Lushan Road, Changsha 410083, People's Republic of China

<sup>2</sup> School of Metallurgical Engineering, Hunan University of Technology, Zhuzhou, Hunan 412008, People's Republic of China

electrospinning, template method, electrochemical method and so on, among which electrochemical deposition is an easy and facile method with low-cost, precisely controllable process and without supplementary catalyst precursor as well as removing the templates [22–25].

In recent years, polypyrrole (PPy), as a kind of conductive macromolecule with nitrogen and carbon atoms co-existing, has attracted lots of attentions ascribing to their good electrical conductivity, ion exchange capacity and easy preparation [26–28]. These excellent attributes make Fe-N-C NFs derived from PPy a very promising nanomaterial used in various application fields, such as catalysts, catalyst supports, sensor, supercapacitor, and so on [26, 29–32]. The transition metals doped within N-C NFs are reported to enhance the electro-catalytic activity of non-precious catalysts at the two following sections: on the one hand, the metal could combine with the other nitrogen atoms, forming  $\text{Me-N}_4$ ,  $\text{Me-N}_2$  or  $\text{Me-N}_x$  active sites [10, 12, 33]; on the other hand, some researchers proposed that the metal itself is not the composition of active sites, but can facilitate the formation of active sites [34, 35]. Based on these factors, Khomenko et al. reported the electro-catalytic activity of PPy for oxygen reduction reaction (ORR) and discussed the possible catalytic mechanism based on a quantum-chemical modeling [36]. And in recent years, the catalytic activity of N-C NFs doped with metallic elements (Fe, Co et al.) and non-metallic elements (such as N and S) have attracted tremendous attentions due to their excellent electrochemical performance, cost-effective and environment-friendly attributes [11, 12, 27, 28, 37, 38].

Traditionally, the catalysts primarily come in the form of powders, and the tedious painting process can inevitably result into catalyst aggregation and catalytic active sites dilution. In our previous paper, the structured CP/Fe-N-CNFs, which was used as electro-chemical catalyst for ORR, was in situ synthesized by CVD [10]. And the high purity pyridinic-N doped platelet CNFs were also synthesized by CVD and heat-treatment under  $\text{NH}_3$  atmosphere [39]. In this paper, the N-C NFs derived from PPy were in situ synthesized on the carbon paper (CP) via electro-chemical polymerization, synthesizing the structured Fe-N-C ANFs/CP. And the effects of iron concentration on the electro-catalytic activity were also investigated.

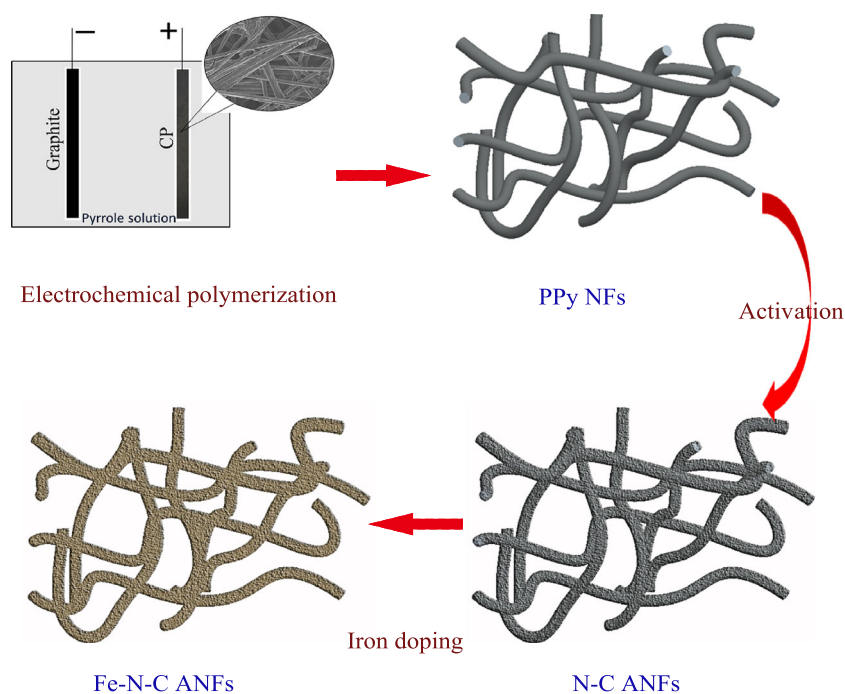
## Experimental section

### Samples preparation

#### Synthesis of PPy NFs in situ grown on carbon paper

In this paper, the polypyrrole nanofibers (PPy NFs) in situ grown on carbon paper (CP) are synthesized according to the following specific procedures: chemical etching, and electrochemical polymerization. Firstly, the homemade CP [40, 41] (the preparation process of CP was reported in our previous paper) was used as PPy NFs in situ grown substrate, which was chemical-etched by 1 M  $\text{HNO}_3$  solution, forming chemical-etched CP with

**Fig. 1** The schematic images of Fe-N-C ANFs synthesis techniques



coarse surface; Secondly, 3.18 g  $\text{Na}_2\text{CO}_3$  and 2.52 g  $\text{NaHCO}_3$  were dissolved into distilled water to form homogenous solution, followed by being added 3.19 g  $\text{LiClO}_4$  and 3.56 g pyrrole monomer, then ultrasonic processing for 1 h to ensure the solute evenly dispersing in the solvent, forming the electrochemical polymerization solution with 0.15 M pyrrole monomer, 0.1 M  $\text{LiClO}_4$  and 0.2 M  $\text{Na}_2\text{CO}_3/\text{NaHCO}_3$ ; thirdly, the pyrrole monomer was in situ electrochemical polymerization on CP using a potentiostat appliance with a double-electrode operating in the synthesized electrochemical polymerization solution. During the electrochemical polymerization process, the graphite electrode was employed as negative electrode and the etched CP was used as the positive electrode, the two electrodes were parallel and 2 cm apart. The electrochemical polymerization current was 0.1 A and time was set as 1, 2, 5, and 10 min, respectively.

At last, the synthesized PPy NFs were washed in deionized water to remove the residual dissociative anions.

### Synthesis of activated N-C NFs derived from PPy on CP

The as-prepared PPy NFs were impregnated in 5 M KOH aqueous solution, followed by heat-treatment in tube furnace and the detailed steps are as follows: firstly, the temperature was heated up to 600 °C with a heating rate of 5 °C/min; secondly, the temperature was kept at 600 °C for 1 h to activate the nanofibers, producing the activated N-C NFs, and the as-synthesized activated N-C NFs were denoted as N-C ANFs.

### Synthesis of N-C ANFs doped with iron on CP

Firstly, the homogenous  $\text{Fe}(\text{NO}_3)_3$  aqueous solution was prepared with different concentration, 0.01 M, 0.03 M, 0.05 M, and 0.10 M; Secondly, the four pieces of CP with N-C

ANFs were impregnated in the prepared  $\text{Fe}(\text{NO}_3)_3$  aqueous solution for 5 h, respectively; Thirdly, the impregnated samples were dried at 80 °C for 1 h and heat-treated as follows: the temperature was heated up to 500 °C with 3 °C/min to make  $\text{Fe}(\text{NO}_3)_3$  decompose completely and then the temperature was elevated to 700 °C, in order to make ferric oxide be reduced under  $\text{H}_2$  atmosphere.

At last, the synthesized N-C ANFs doped with iron were washed in 0.1 M HCl to remove the residual metal and then washed in deionized water till neutral. The as-prepared N-C ANFs doped with iron were abbreviated as Fe-N-C ANFs and Fe-N-C ANFs prepared with 0.01 M, 0.03 M, 0.05 M, 0.10 M  $\text{Fe}(\text{NO}_3)_3$  aqueous solution were denoted as 0.01-Fe-N-C ANFs, 0.03-Fe-N-C ANFs, 0.05-Fe-N-C ANFs, and 0.10-Fe-N-C ANFs, respectively. The synthesis process of Fe-N-C ANFs is visually described in Fig. 1.

## Characterization

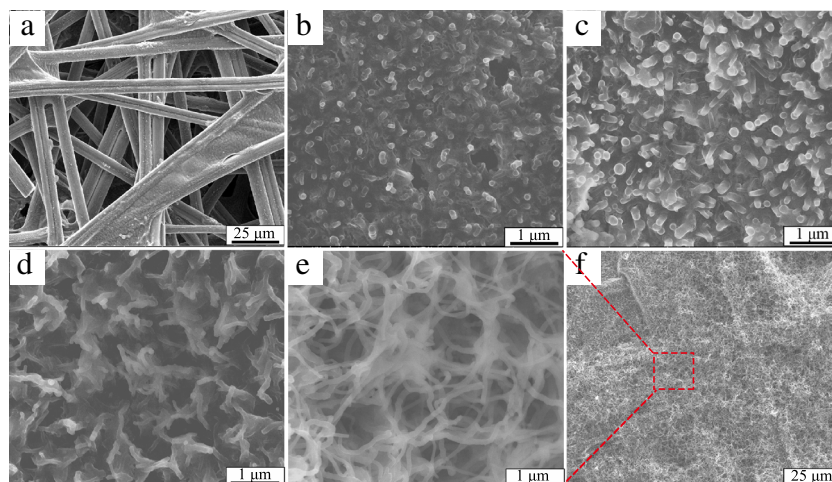
### Morphology and microstructure characterization

The morphology and element content analysis are represented by scanning electron microscope (SEM, JEOL JSM-7600F) and energy dispersive spectrometer (EDS). The microstructures are observed by transmission electron microscopy (TEM, JEM-2100F). The chemical states and element content are characterized by an X-ray photoelectron spectroscopy (XPS) apparatus (Thermo Scientific K-Alpha) equipped with a monochromatic Al  $K_{\alpha}$  X-ray source of 1486.6 eV.

### Electro-chemical characterization

The electrochemical activity of the samples are characterized by an electrochemical workstation (CHI 660e, Shanghai Chenhua Instrument Co. Ltd., China). The Cyclic

**Fig. 2** The SEM images of **a** the home-made CP and electrochemical polymerized PPy NFs with different time, **b** 1 min, **c** 2 min, **d** 5 min, **e** and **f** 10 min



voltammetry (CV) and Linear Sweep Voltammetry (LSV) are carried out at room temperature (25 °C) in a conventional three-electrode electro-chemical cell with platinum electrode as counter electrode, Hg/HgO electrode as reference electrode and the prepared Fe-N-C ANFs as working electrode. The CV and LSV spectra are tested in O<sub>2</sub> or N<sub>2</sub> saturated 0.1 M KOH aqueous solution. Rotating disk electrode (RDE) (AFMSRCE) voltammetry measurements and amperometric *i-t* curves were carried out at the same condition. Before the experiments, the glassy carbon (GC) electrode was carefully polished, then washed with distilled water for double times, ethanol solution once and dried in vacuum. The Fe-N-C ANFs were scraped gently from CP substrate, then 3.5 mg scraped Fe-N-C ANFs powders were mixed with 1.0 ml solution (the ratio of distill water with nafion is 9:1) under ultrasonic process. A certain amount of the Fe-N-C ANFs (15 μl) is dropped onto the GC electrode. For comparison, a commercial catalyst of 3.5 mg/ml 20% Pt/C suspension is synthesized according to the same procedure as above.

## Results and discussions

SEM images of PPy NFs with different electrochemical polymerization time (1, 2, 5, and 10 min, respectively) are exhibited in Fig. 2. Figure 2a shows that home-made CP [40–42] is composed of the carbon fibers with a diameter of 7 μm and matrix carbon, which was fabricated via curing, pressing, carbonization, and graphitization process, so that the home-made CP possesses good electrical conductivity. In this paper, we chose the home-made CP as substrate for in situ electrochemical polymerizing PPy NFs. It can be seen that the nucleation of smallish PPy NFs have occurred (Fig. 2b) in the initial period of electrochemical polymerization and then the nucleus turn to grow up mainly along one-dimensional direction as time extends, as shown in Fig. 2c–e. The images show that the morphology differences of PPy NFs are not obvious except for the length, which can also confirm that the PPy NFs have only grown along with the axial direction. At last, the in situ electrochemical polymerized PPy NFs have covered the CP substrate almost completely and homogeneously with length of tens of microns, as shown in Fig. 2f.

Figure 3 shows the morphology and microstructure differences between PPy NFs before and after activation, namely, the PPy NFs and N-C ANFs (Fig. 3). It is shown that the specific surface area increases obviously from PPy NFs (68.52 m<sup>2</sup> g<sup>-1</sup>) to N-C ANFs (82.16 m<sup>2</sup> g<sup>-1</sup>). Meantime, the diameter decreases from PPy NFs (Fig. 3a and a inset) to N-C ANFs (Fig. 3b and b inset), which could also be confirmed by TEM images of PPy NFs and N-C ANFs (Fig. 3c, d). It can be seen some defects and

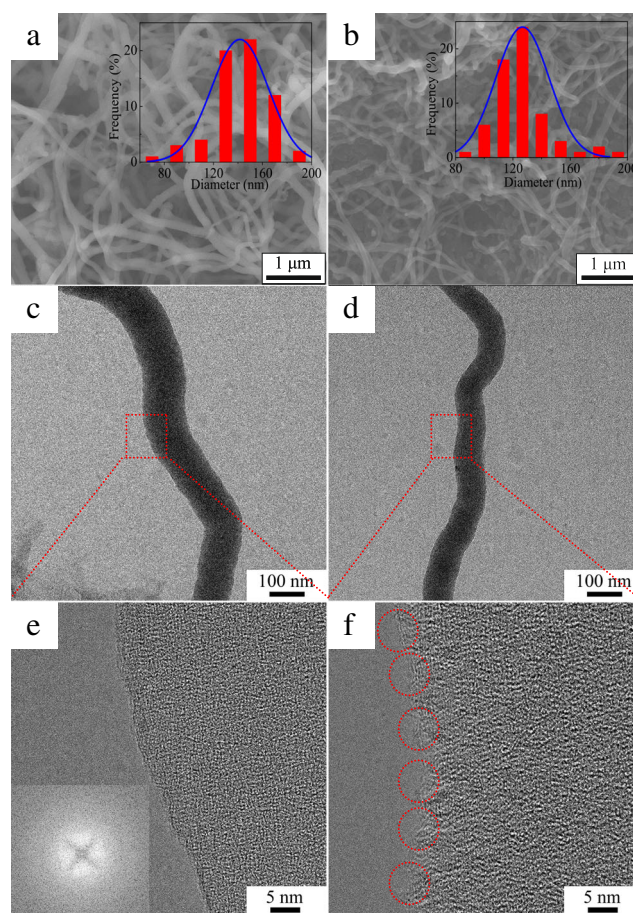


**Fig. 3** SEM, TEM and HRTEM images of PPy NFs and N-C ANFs. SEM images of **a** before and **b** after KOH activation, the corresponding insets are the normal distribution of nanofiber diameter; TEM images of **c** before and **d** after KOH activation, and the corresponding HRTEM images (the red dashed rectangles in **c** and **d**) of **e** before and **f** after KOH activation, the **e** inset is the diffraction pattern of the amorphous carbon in PPy NFs

pores at the boundary sites of N-C ANFs ascribing to the KOH activation (red dashed circles in Fig. 3f) compared to boundary sites of PPy NFs (Fig. 3e), which is in an accordance with the the specific surface area results. Moreover, it is shown obviously that the PPy NFs and N-C ANFs both exhibit an amorphous type (Fig. 3e, and f), which could also be proved by the diffraction pattern (Fig. 3e inset).

SEM images of Fe-N-C ANFs pre-treated with different Fe(NO<sub>3</sub>)<sub>3</sub> precursor concentration are shown in Fig. 4. Seen from SEM images, there are no significant morphology differences between 0.01-Fe-N-C ANFs and 0.03-Fe-N-C ANFs (Fig. 4a, b), in which only fibrous Fe-N-C ANFs could be seen on CP substrate without iron-containing particles. While, as Fe(NO<sub>3</sub>)<sub>3</sub> precursor concentration increases, it is observed that few iron-containing nanoparticles could be observed in 0.05-Fe-N-C ANFs, as labeled by the red dashed circles in Fig. 4c. When

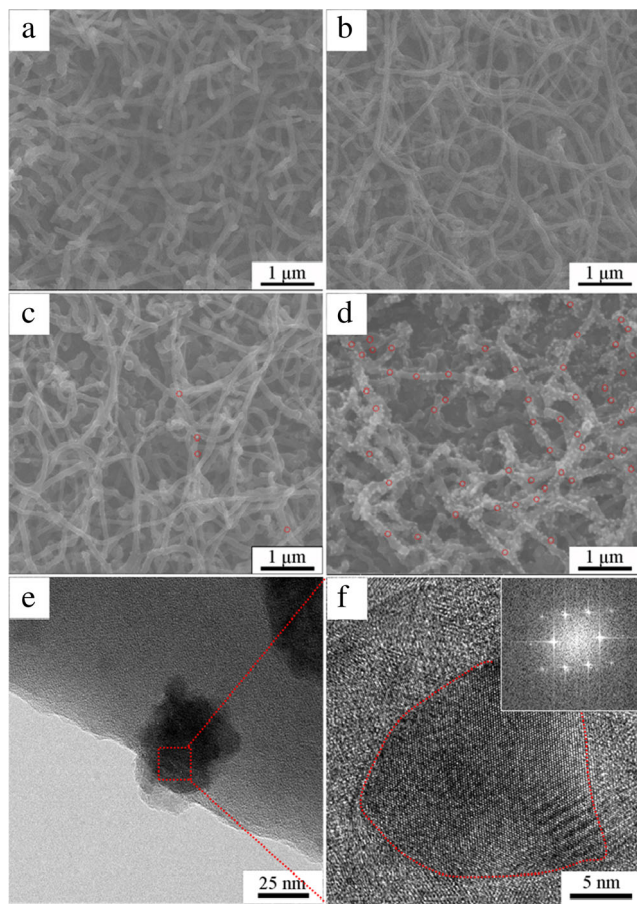


**Fig. 4** SEM, TEM, and HRTEM images of the Fe-N-C ANFs. SEM images of **a** 0.01-Fe-N-C ANFs, **b** 0.03-Fe-N-C ANFs, **c** 0.05-Fe-N-C ANFs, and **d** 0.10-Fe-N-C ANFs; **e** TEM images of 0.05-Fe-N-C ANFs; **f** HRTEM images of the red dashed rectangle in **e** and the **f** inset is diffraction pattern of the iron-containing nanoparticle

$\text{Fe}(\text{NO}_3)_3$  precursor concentration reaches up to 0.10 M, many iron-containing nanoparticles can be seen in 0.10-Fe-N-C ANFs (Fig. 4d red dashed circles). The reason could be speculated that the precursor component distributes nonuniformly on N-C ANFs when  $\text{Fe}(\text{NO}_3)_3$  precursor concentration is high, as a result obtaining many visible iron-containing nanoparticles (Fig. 4d). TEM image shows that the iron-containing nanoparticles are combined well with the surrounding nanofiber (Fig. 4e), which could be also proved by the HRTEM image in Fig. 4f, namely, the iron-containing nanoparticle has bonding combining with the surrounding amorphous structure. Furthermore, the HRTEM image (Fig. 4f) and the diffraction pattern (Fig. 4f inset) of the iron-containing nanoparticles exhibit that it shows good crystallization characteristic of iron-containing nanoparticles, which could change the electron structure of the surrounding carbon and nitrogen atoms and then improve the electro-chemical activity of the N-C ANFs.

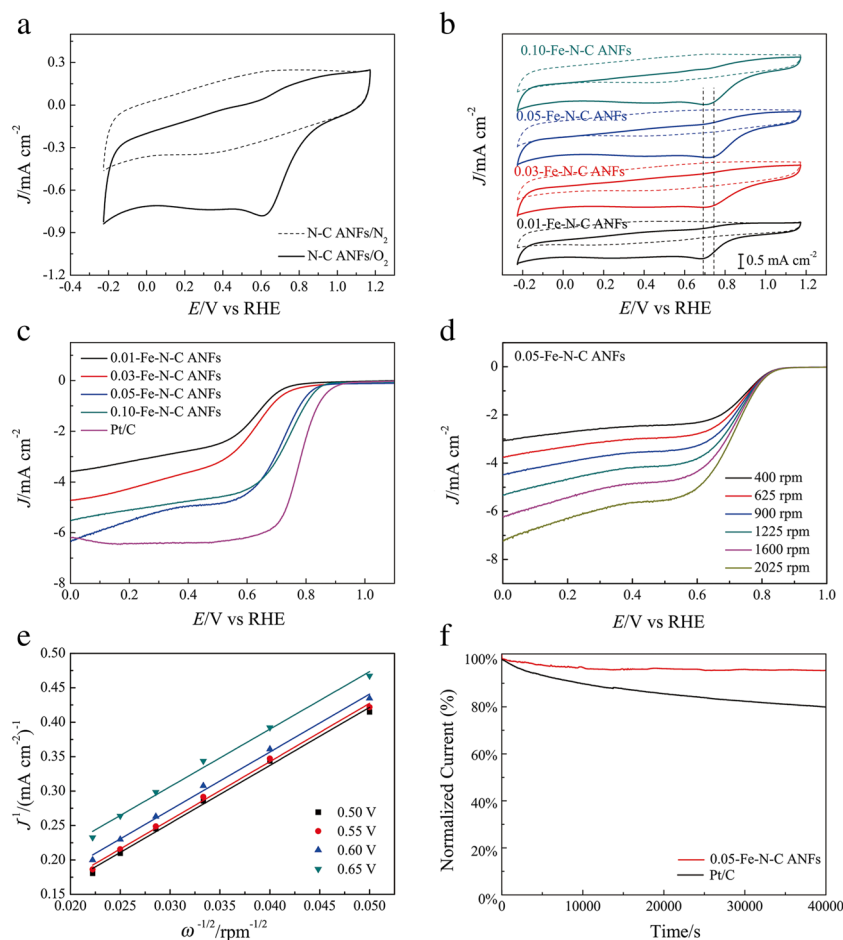
The electrochemical performances of 0.01-Fe-N-C ANFs, 0.03-Fe-N-C ANFs, 0.05-Fe-N-C ANFs, and 0.10-Fe-N-C ANFs are investigated in 0.1 M  $\text{O}_2/\text{N}_2$ -saturated KOH solution via cyclic voltammetry (CV), rotating disk electrode (RDE) voltammetry curves and amperometric  $i$ - $t$  curves (Fig. 5). The obvious oxygen reduction peak could be observed in N-C ANFs (Fig. 5a) and Fe-N-C ANFs (Fig. 5b), indicating their electro-catalytic activity for oxygen reduction. As seen in Fig. 5b, Fe-N-C ANFs show significant positive shifts in onset-potential and peak potential, compared to those of N-C ANFs. Also, it is indicated that no obvious reduction peaks are observed in CV spectra measured in  $\text{N}_2$ -saturated 0.1 M KOH solution, appearing a tilted rectangular shape. This is due to the influence of the ohmic resistance from electrolyte motion in carbon pores on the mechanism of double-layer formation [43, 44]. Considering the effect of double-layer capacitance on the electrochemical performance of the electrocatalysts, the LSV spectra in Fig. 5c, d have been removed the capacitance effect. It shows that 0.05-Fe-N-C ANFs and 0.10-Fe-N-C ANFs reveal much higher onset-potential (0.89 V) than that of 0.01-Fe-N-C ANFs and 0.03-Fe-N-C ANFs (Fig. 5c). Fig. 5d shows the RDE curves of 0.05-Fe-N-C ANFs with different rotation speeds in 0.1 M  $\text{O}_2/\text{N}_2$ -saturated KOH solution and Fig. 5e shows four linear K-L plots near parallelism at different potentials, suggesting first-order reaction kinetics towards the concentration of dissolved oxygen on 0.05-Fe-N-C ANFs. The numbers of transferred electron can be calculated by the following K-L equation [13, 45]:

$$\frac{1}{J} = \frac{1}{B\omega^{0.5}} + \frac{1}{J_k} \quad (1)$$

$$B = 0.62nFC_oD_o^{2/3}v^{-1/6} \quad (2)$$

Where  $J$  is the observed current density,  $J_k$  denotes the kinetic-limit current density,  $B$  is the Levich slope,  $\omega$  is the rotating rate;  $n$  is the number of electrons transferred per  $\text{O}_2$ ,  $F = 96485 \text{ C mol}^{-1}$ ,  $C_o = 1.2 \times 10^{-6} \text{ mol cm}^{-3}$ ,  $D_o = 1.9 \times 10^{-5} \text{ cm}^2 \text{ s}^{-1}$ , and  $v = 0.01 \text{ cm}^2 \text{ s}^{-1}$ . The numbers of transferred electrons of 0.05-Fe-N-C ANFs calculated via the slopes of the plots of  $J^{-1}$  versus  $\omega^{-1/2}$  are 3.34, 3.33, 3.35, and 3.37 at 0.50, 0.55, 0.60, and 0.65 V, respectively. It reveals a mixed two electron and four electron transfer process and the steadier electron transfer numbers indicate a smoother and more electrochemically stable ORR process over 0.05-Fe-N-C ANFs. To some extent, introducing metal into carbon-nitrogen materials could enhance the electro-catalytic activity for ORR, which is ascribing to the generation of active sites  $\text{Fe-N}_x$  with the introduction of iron element. Basically, if we observe  $n$  is larger than 3, which means that the material supports 4-electron pathway with slow final steps. As a result,  $n$  should be 4 when we calculate  $J_k$  using the Eq. 1, and

**Fig. 5** The electro-chemical activity of the as-prepared samples in 0.1 M KOH electrolyte. **a** CV of N-C ANFs tested in  $O_2/N_2$  saturated 0.1 M KOH solution with scan rate of  $10 \text{ mV s}^{-1}$ ; **b** CV of 0.01-Fe-N-C ANFs, 0.03-Fe-N-C ANFs, 0.05-Fe-N-C ANFs and 0.10-Fe-N-C ANFs in  $O_2/N_2$  saturated 0.1 M KOH solution; **c** LSV curves of Fe-N-C ANFs and Pt/C at rotation speed of 1600 rpm; **d** RDE voltammetry curves for ORR at rotation speeds ranging from 400 to 2025 rpm; **e** the K-L plots of 0.05-Fe-N-C ANFs at 0.50 V, 0.55 V, 0.60 V, and 0.65 V; **f** The Amperometric  $i-t$  curves of 0.05-Fe-N-C ANFs and Pt/C at 0.6 V in  $O_2$  saturated 0.1 M KOH solution



in this way, the calculated  $J_k$  of the 0.05-Fe-N-C ANFs and 0.10-Fe-N-C ANFs at 0.8 V (vs RHE) ( $0.68 \text{ mA cm}^{-2}$  and  $1.03 \text{ mA cm}^{-2}$ , respectively) are much larger than that of 0.01-Fe-N-C ANFs ( $0.12 \text{ mA cm}^{-2}$ ) and 0.03-Fe-N-C ANFs ( $0.22 \text{ mA cm}^{-2}$ ). Additionally, the mass  $J_k$  at 0.8 V (vs RHE) of 0.01-Fe-N-C ANFs, 0.03-Fe-N-C ANFs, 0.05-Fe-N-C ANFs and 0.10-Fe-N-C ANFs are  $0.46 \text{ A g}^{-1}$ ,

$0.82 \text{ A g}^{-1}$ ,  $2.55 \text{ A g}^{-1}$  and  $3.84 \text{ A g}^{-1}$ , respectively. The mass  $J_k$  of 0.05-Fe-N-C ANFs and 0.10-Fe-N-C ANFs at 0.8 V are comparable with that of Fe-N/C catalysts in literatures [46]. Moreover, the durability of 0.05-Fe-N-C ANFs was measured at a constant voltage for 40,000 s in  $O_2$  saturated 0.1 M KOH electrolyte, and the  $i-t$  curves reveal that 0.05-Fe-N-C ANFs present a small fluctuation

**Fig. 6** The SEM images of 0.05-Fe-N-C ANFs **a** before and **b** after the electro-chemical tests

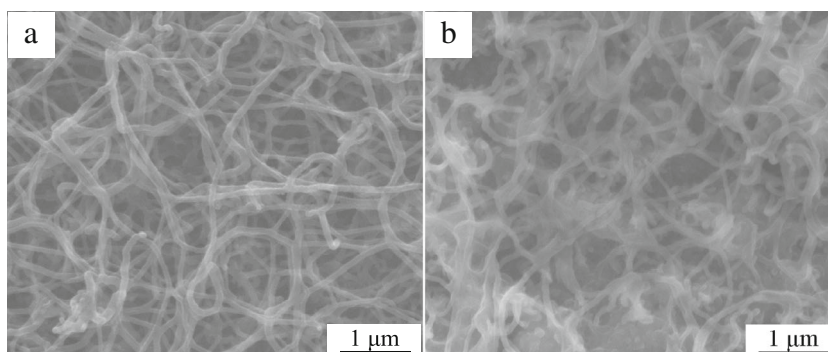
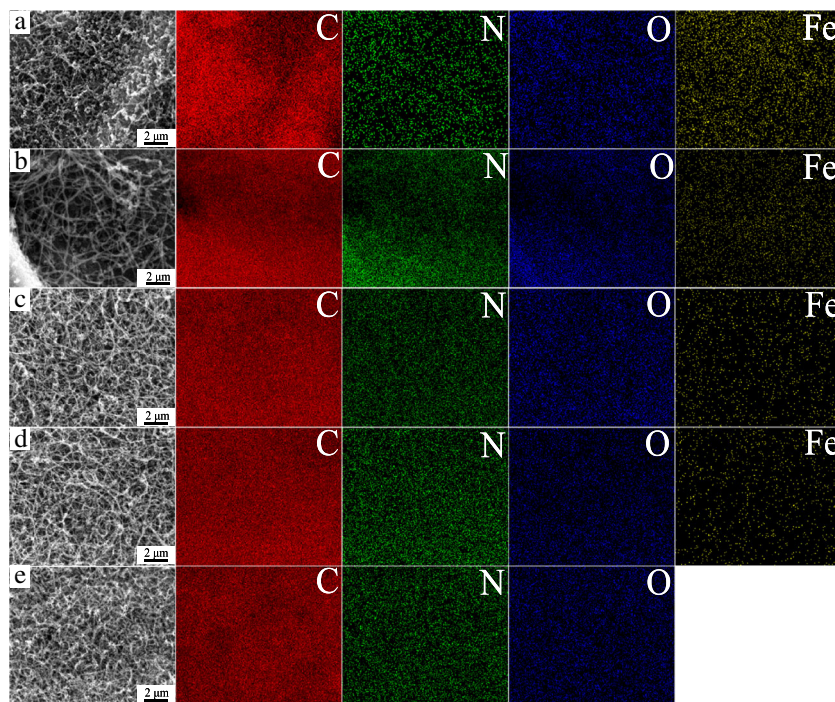


**Fig. 7** The SEM mapping images of **a** 0.10-Fe-N-C ANFs, **b** 0.05-Fe-N-C ANFs, **c** 0.03-Fe-N-C ANFs, **d** 0.01-Fe-N-C ANFs, and **e** N-C ANFs. The corresponding C element, N element, O element, and Fe element mapping images are also shown in the figure



(95.56%) after 40,000 s, while the normalized current of Pt/C decreases to approximately 79.93% after 40,000 s (Fig. 5f).

As a result, on the one hand, the catalytic activity of Fe-N-C ANFs enhances with iron concentration increases, namely 0.01-Fe-N-C ANFs to 0.05-Fe-N-C ANFs, which can be explained that the Fe-N<sub>x</sub> active sites increase correspondingly; on the other hand, with iron concentration continuously increasing in 0.10-Fe-N-C ANFs sample,

its catalytic activity does not increase monotonously, which could be ascribing to the bulk agglomeration of iron-containing nanoparticles, resulting in the active sites aggregation and inhomogeneous.

The SEM morphologies of 0.05-Fe-N-C ANFs before and after the electro-chemical tests are shown in Fig. 6. It is observed that the structure of the one-dimensional Fe-N-C ANFs can be basically maintained, that is to say, the microstructure of the 0.05-Fe-N-C ANFs after ORR in 0.1 M

**Fig. 8** XPS spectra of Fe-N-C ANFs. **a** XPS full spectra, **b** N 1s XPS spectra, and **c** Fe 2p XPS spectra of 0.01-Fe-N-C ANFs, 0.03-Fe-N-C ANFs, 0.05-Fe-N-C ANFs, and 0.10-Fe-N-C ANFs, respectively

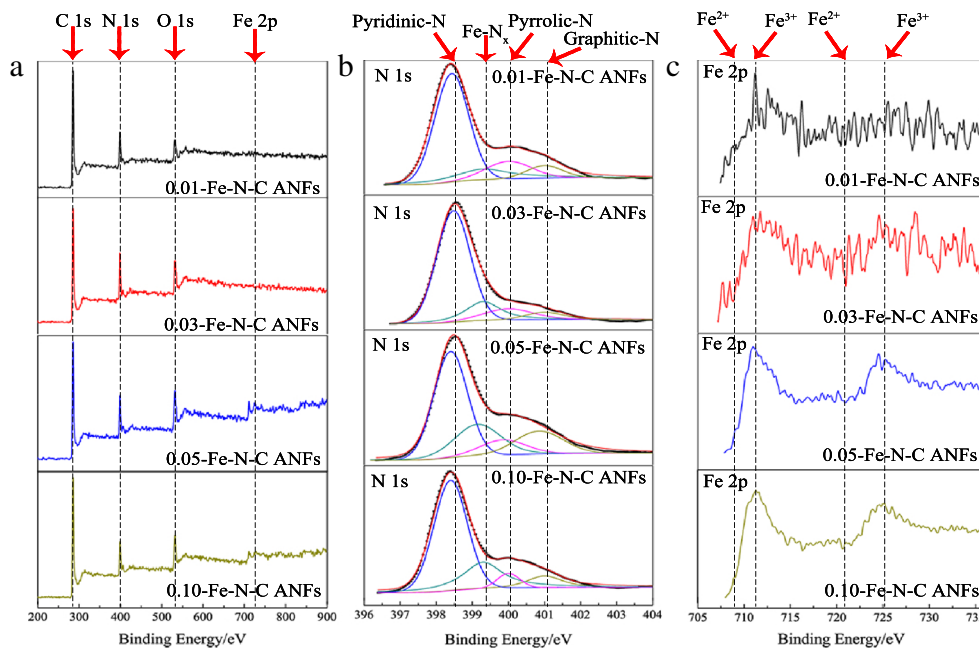


**Table 1** C, N, Fe, and O content in the as-prepared samples, and No. 1, 2, 3, and 4 represent the 0.01-Fe-N-C ANFs, 0.03-Fe-N-C ANFs, 0.05-Fe-N-C ANFs, and 0.10-Fe-N-C ANFs, respectively

No.	C (at.%)	N (at.%)	N <sub>pyr</sub> (at.%)	N <sub>Fe-N<sub>x</sub></sub> (at.%)	N <sub>N-H</sub> (at.%)	N <sub>g</sub> (at.%)	Fe (at.%)	O (at.%)
1	78.11	16.98	11.48	1.09	2.92	1.49	0.36	4.55
2	77.36	16.07	10.19	2.41	2.24	1.23	0.58	5.99
3	75.15	15.30	7.66	3.85	1.46	2.33	1.63	7.92
4	74.58	15.70	10.20	3.15	1.14	1.22	2.08	7.64

KOH solution was not destroyed, suggesting good durability in another point of view.

SEM mapping images of the 0.01-Fe-N-C ANFs, 0.03-Fe-N-C ANFs, 0.05-Fe-N-C ANFs, and 0.10-Fe-N-C ANFs (Fig. 7) show that the carbon, nitrogen, oxygen, and iron elements distribute on N-C ANFs homogeneously and almost non-aggregation. Moreover, it could be seen that the Fe concentration gradually decreases from 0.10-Fe-N-C ANFs to 0.01-Fe-N-C ANFs, and only a few agglomerated iron-containing nanoparticles appear in 0.10-Fe-N-C ANFs (Fig. 7a), while there are no aggregations in the other as-prepared samples.

To figure out the N, and Fe bonding configurations in 0.01-Fe-N-C ANFs, 0.03-Fe-N-C ANFs, 0.05-Fe-N-C ANFs, and 0.10-Fe-N-C ANFs, we investigated their X-ray photoelectron spectroscopy (XPS), as shown in Fig. 8. It can be seen that carbon, nitrogen, oxygen, and iron element characteristic-peaks appear in the XPS total spectra, as shown in Fig. 8. The corresponding element concentration is listed in Table 1, from which it could be found that the changes of carbon and nitrogen element concentration are ruleless, while iron element concentration monotonously increasing from 0.01 to 0.10 M. In addition, the C 1s and N 1s XPS spectra are also analyzed to investigate the changes of the bonding configurations and it could be observed that N 1s XPS spectra of the Fe-N-C ANFs can be deconvoluted into four types according to the binding energy: pyridinic-N (N<sub>pyr</sub>, 398.4 eV), Fe-N<sub>x</sub> (N<sub>Fe-N<sub>x</sub></sub>, 399.3 eV), pyrrolic-N (N<sub>N-H</sub>, 400 eV), and graphitic-N (N<sub>g</sub>, 401 eV) [47]. It is exhibited that the concentration of Fe-N<sub>x</sub> group first increases, then decreases along with the iron element concentration increases from 0.01-Fe-N-C ANFs to 0.10-Fe-N-C ANFs, which is in agreement with the electro-catalytic activity for ORR of the as-prepared samples. As a result, the Fe-N<sub>x</sub> groups could be the electro-catalytic active sites for ORR instead of Fe.

## Conclusions

To sum it up, the structured Fe-N-C ANFs/CP (The activated polypyrrole nanofibers doped with iron element in-situ electro-chemical polymerization on the home-made carbon paper (CP)) was synthesized by electrochemical

polymerization. And the 0.05-Fe-N-C ANFs exhibit more positive onset-potential and higher peak current density than those of 0.01-Fe-N-C ANFs, 0.03-Fe-N-C ANFs, and 0.10-Fe-N-C ANFs, revealing superior electro-catalytic activity for ORR, which could be ascribing to higher Fe-N<sub>x</sub> concentration, and well-dispersed as well as undiluted catalytic active sites. Meanwhile, 0.05-Fe-N-C ANFs show better alkaline tolerance than the commercial Pt/C catalyst. However, the catalytic activity of the Fe-N-C ANFs is much poorer than that of the commercial Pt/C catalyst, which could be ascribing to the low catalytic active-site concentration.

**Acknowledgements** The authors gratefully acknowledge financial support from the National Key Research and Development Program of China (No. 2016YFB0101310).

## References

1. Hebling C, Heinzel A, Golombowski D, Meyer T, Müller M, Zedda M (2002) Fuel cells for low power applications. *J Power Sources* 105:250–255
2. Vignarooban K, Lin J, Arvay A, Kolli S, Kruusenberg I, Tammeveski K, Munukutla L, Kannan AM (2015) Nano-electrocatalyst materials for low temperature fuel cells: a review. *Chin J Catal* 36:458–472
3. Authayanun S, Im-Orb K, Arpornwichanop A (2015) A review of the development of high temperature proton exchange membrane fuel cells. *Chin J Catal* 36:473–483
4. Li Y, Xu H, Zhao H, Lu L, Sun X (2016) Improving the durability of Pt/C catalyst in PEM fuel cell by doping vanadium phosphate oxygen. *J Appl Electrochem* 46:183–189
5. Yu S, Wang Y, Zhu H, Wang Z, Han K (2016) Synthesis and electrocatalytic performance of phosphotungstic acid-modified Ag@Pt/MWCNTs catalysts for oxygen reduction reaction. *J Appl Electrochem* 46:917–928
6. Videla AHAM, Zhang L, Kim J, Zeng J, Francia C, Zhang J, Specchia S (2013) Mesoporous carbons supported non-noble metal FeN<sub>x</sub> electrocatalysts for PEM fuel cell oxygen reduction reaction. *J Appl Electrochem* 43:159–169
7. Yu-Ping LI, Jiang LH, Wang SL, Sun GQ (2016) Multi-scaled carbon supported platinum as a stable electrocatalyst for oxygen reduction reaction. *J Electrochem* 22:135–146
8. Ammam M, Easton EB (2013) Oxygen reduction activity of binary PtMn/C, ternary PtMnX/C (X = Fe, Co, Ni, Cu, Mo and, Sn) and quaternary PtMnCuX/C (X=Fe, Co, Ni, and Sn) and PtMnMoX/C (X=Fe, Co, Ni, Cu and Sn) alloy catalysts. *J Power Sources* 236:311–320



9. Rego R, Oliveira C, Velázquez A, Cabot PL (2010) A new route to prepare carbon paper-supported Pd catalyst for oxygen reduction reaction. *Electrochem Commun* 12:745–748
10. Sun M, Xie Z, Wu X, Deng X, Liu C, Huang Q, Huang B (2017) The synthesis and electro-catalytic activity for ORR of the structured electrode material: CP/Fe-N-CNFs. *J Solid State Electrochem*
11. Si YJ, Chen CG, Wei Y, Cai H (2011) The synthesis and characterization of a Co-N/C composite catalyst for the oxygen reduction reaction in acidic solution. *Chin Sci Bull* 56:1086–1091
12. Shi Z, Liu H, Lee K, Dy E, Chlistunoff J, Blair M, Zelenay P, Zhang J, Liu ZS (2011) Theoretical study of possible active site structures in cobalt- polypyrrole catalysts for oxygen reduction reaction. *J Phys Chem C* 115:16672–16680
13. Qu L, Liu Y, Baek JB, Dai L (2010) Nitrogen-doped graphene as efficient metal-free electrocatalyst for oxygen reduction in fuel cells. *ACS Nano* 4:1321–1326
14. Wang S, Dai C, Li J, Zhao L, Ren Z, Ren Y, Qiu Y, Yu J (2015) The effect of different nitrogen sources on the electrocatalytic properties of nitrogen-doped electrospun carbon nanofibers for the oxygen reduction reaction. *Int J Hydrog Energy* 40:4673–4682
15. Choi CH, Chung MW, Park SH, Woo SI (2013) Additional doping of phosphorus and/or sulfur into nitrogen-doped carbon for efficient oxygen reduction reaction in acidic media. *Phys Chem Chem Phys (PCCP)* 15:1802–1805
16. Yao X, Li K, Ye J, Shao QY (2016) First principles study on B/N pairs co-doping zigzag single-walled carbon nanotubes. *Chem Phys Lett* 653:144–148
17. Domínguez C, Pérez-Alonso FJ, Al-Thabaiti SA, Basahel SN, Obaid AY, Alyoubi AO, Fuente JLGDL, Rojas S (2015) Effect of N and S co-doping of multiwalled carbon nanotubes for the oxygen reduction. *Electrochim Acta* 157:158–165
18. Sheng ZH, Shao L, Chen JJ, Bao WJ, Wang FB, Xia XH (2011) Catalyst-free synthesis of nitrogen-doped graphene via thermal annealing graphite oxide with melamine and its excellent electrocatalysis. *ACS Nano* 5:4350–4358
19. Subramanian NP, Li X, Nallathambi V, Kumaraguru SP, Colon-Mercado H, Gang W, Lee JW, Popov BN (2009) Nitrogen-modified carbon-based catalysts for oxygen reduction reaction in polymer electrolyte membrane fuel cells. *J Power Sources* 188:38–44
20. Sheng J, Ma C, Ma Y, Zhang H, Wang R, Xie Z, Shi J (2016) Synthesis of microporous carbon nanofibers with high specific surface using tetraethyl orthosilicate template for supercapacitors. *Int J Hydrog Energy* 41:9383–9393
21. Liu Q, Cui ZM, Ma Z, Bian S, Song WG (2008) Highly active and stable material for catalytic hydrodechlorination using ammonia-treated carbon nanofibers as Pd supports. *J Phys Chem C* 112:1199–1203
22. Park ES, Park HK, Park HS, Lee CS (2015) Synthesis and electrochemical properties of CNFs-Si composites as an anode material for Li secondary batteries. *J Nanosci Nanotechnol* 15:8961–8970
23. Chen C, Lu Y, Ge Y, Zhu J, Jiang H, Li Y, Hu Y, Zhang X (2016) Synthesis of nitrogen-doped electrospun carbon nanofibers as anode material for high-performance sodium-ion batteries. *Energy Technol* 4:1440–1449
24. Hsieh CT, Chen JM, Huang YH, Kuo RR, Li CT, Shih HC, Lin TS, Wu CF (2006) Influence of fluorine/carbon atomic ratio on superhydrophobic behavior of carbon nanofiber arrays. *J Vac Sci Technol B* 24:113–117
25. Zhang Y, Xu Y, Suhir E, Gu C, Liu X (2008) Compliance properties study of carbon nanofibres (CNFs) array as thermal interface material. *J Phys D Appl Phys* 41:155105–1–5
26. Lee H, Kim H, Mi SC, Choi J, Lee Y (2011) Fabrication of polypyrrole (PPy)/carbon nanotube (CNT) composite electrode on ceramic fabric for supercapacitor applications. *Electrochim Acta* 56:7460–7466
27. Yao T, Cui T, Fang X, Yu J, Cui F, Wu J (2013) Preparation of yolk/shell Fe<sub>3</sub>O<sub>4</sub>@polypyrrole composites and their applications as catalyst supports. *Chem Eng J* 225:230–236
28. Oh HS, Oh JG, Roh B, Hwang I, Kim H (2011) Development of highly active and stable non-precious oxygen reduction catalysts for PEM fuel cells using polypyrrole and a chelating agent. *Electrochem Commun* 13:879–881
29. Yuan Y, Zhou S, Li Z (2010) Polypyrrole/carbon black composite as a novel oxygen reduction catalyst for microbial fuel cells. *J Power Sources* 195:3490–3493
30. Qiu L, Peng Y, Liu B, Lin B, Peng Y (2012) Polypyrrole nanotube-supported gold nanoparticles: an efficient electrocatalyst for oxygen reduction and catalytic reduction of 4-nitrophenol. *Appl Catal A Gen* 413:230–237
31. Zhao H, Li L, Yang J, Zhang Y (2008) Nanostructured polypyrrole/carbon composite as Pt catalyst support for fuel cell applications. *J Power Sources* 184:375–380
32. Wang Y, Jia W, Strout T, Schempf A, Zhang H, Li B, Cui J, Lei Y (2010) Ammonia gas sensor using polypyrrole-coated TiO<sub>2</sub>/ZnO nanofibers. *Electroanalysis* 21:1432–1438
33. Koslowski UI, Wurmbach IA, Fiechter S, Bogdanoff P (2008) Nature of the catalytic centres of porphyrin based electrocatalysts for the ORR—a correlation of kinetic current density with the site density of Fe-N<sub>4</sub> centres. *J Phys Chem C J Phys Chem C* 112:15356–15366
34. Nallathambi V, Lee JW, Kumaraguru SP, Gang W, Popov BN (2008) Development of high performance carbon composite catalyst for oxygen reduction reaction in PEM Proton Exchange Membrane fuel cells. *J Power Sources* 183:34–42
35. Matter PH, Wang E, Ozkan US (2006) Preparation of nanostructured nitrogen-containing carbon catalysts for the oxygen reduction reaction from SiO<sub>2</sub> - and MgO-supported metal particles. *J Catal* 243:395–403
36. Khomenko VG, Barsukov VZ, Katashinskii AS (2005) The catalytic activity of conducting polymers toward oxygen reduction. *Electrochim Acta* 50:1675–1683
37. Chen X, Li F, Wang X, Sun S, Xia D (2012) Density functional theory study of the oxygen reduction reaction on a Cobalt-Polypyrrole Composite Catalyst. *J Phys Chem C* 116:12553–12558
38. Ren S, Guo Y, Ma S, Mao Q, Wu D, Yang Y, Jing H, Song X, Hao C (2017) Co<sub>3</sub>O<sub>4</sub> nanoparticles assembled on polypyrrole/graphene oxide for electrochemical reduction of oxygen in alkaline media. *Chin J Catal* 38:1281–1290
39. Sun M, Wu X, Xie Z, Deng X, Wen J, Huang Q, Huang B (2017) Tailoring platelet carbon nanofibers for high-purity pyridinic-N doping: a novel method for synthesizing oxygen reduction reaction catalysts. *Carbon*
40. Xie ZY, Jin GY, Zhang M, Zhe-An SU, Zhang MY, Chen JX, Huang QZ (2010) Improved properties of carbon fiber paper as electrode for fuel cell by coating pyrocarbon via CVD method. *Chin J Nonferrous Met* 20:1412–1417
41. Xie Z, Tang X, Yang P, Sun M, Yang K, Huang Q (2015) Carboxyl-terminated butadiene-acrylonitrile-modified carbon paper for use of gas diffusion layer in PEM fuel cells. *Int J Hydrog Energy* 40:14345–14352
42. Yang K, Xie ZY, Huang QZ, Tang X, Hu R (2014) Fabrication and characterization of carbon fiber paper for application of proton exchange membrane fuel cells. *Mater Sci Forum* 787:407–411

43. Dhanya P, Aravindan V, Srinivasan M, Ogale S (2014) 3D micro-porous conducting carbon beehive by single step polymer carbonization for high performance supercapacitors: the magic of in situ porogen formation. *Energy Environ Sci* 7:728–735
44. Lee D, Jung JY, Park MS, Lee YS (2014) Preparation of novolac-type phenol-based activated carbon with a hierarchical pore structure and its electric double-layer capacitor performance. *Carbon Lett* 15:192–197
45. Wang D, Xin HL, Hovden R, Wang H, Yu Y, Muller DA, Disalvo FJ, Abruña HD (2013) Structurally ordered intermetallic platinum–cobalt core–shell nanoparticles with enhanced activity and stability as oxygen reduction electrocatalysts. *Nat Mater* 12:81–87
46. Chen X, He F, Shen Y, Yang Y, Mei H, Liu S, Mori T, Zhang Y (2017) Effect of carbon supports on enhancing mass kinetic current density of Fe-N/C electrocatalysts. *Chem A Eur J* 23:14597–14603
47. Kothandaraman R, Nallathambi V, Artyushkova K, Barton SC (2009) Non-precious oxygen reduction catalysts prepared by high-pressure pyrolysis for low-temperature fuel cells. *Appl Catal B-Environ* 92:209–216